

The Deep SWIRE Field

I. 20cm Continuum Radio Observations: A Crowded Sky

Frazer N. Owen,¹ & G. E. Morrison,^{2,3}

ABSTRACT

We present results from deep radio observations taken with the VLA at a center frequency of 1400 MHz covering a region of the SWIRE Spitzer Legacy survey, centered at $10^h46^m00^s$, $59^\circ01'00''$ (J2000). The reduction and cataloging of radio sources are described. An electronic catalog of the sources detected above 5 sigma is also presented.

The survey presented is the deepest so far in terms of the radio source density on the sky. Perhaps surprisingly, the sources down to the bottom of the catalog appear to have median angular sizes still > 1 arcsecond, like their cousins 10-100 times stronger. The shape of the differential log N - log S counts also seems to require a correction for the finite sizes of the sources to be self-consistent. If the log N - log S normalization remains constant at the lowest flux densities, there are about 6 sources per square arcminute at $15 \mu\text{Jy}$ at 20cm. Given the finite source size this implies that we may reach the natural confusion limit near $1 \mu\text{Jy}$.

Subject headings: cosmology: observations — galaxies: evolution — galaxies: starburst — infrared: galaxies galaxies

1. Introduction

Understanding the growth and evolution of galaxies is one of the key goals of modern astronomy. A new generation of multi-wavelength surveys from X-ray to radio wavelengths are providing the starting point for new leaps of understanding of the subject. The key has

¹National Radio Astronomy Observatory, P. O. Box O, Socorro, NM 87801 USA.; fowen@nrao.edu The National Radio Astronomy Observatory is facility of the National Science Foundation operated under cooperative agreement by Associated Universities Inc.

²Institute for Astronomy, University of Hawaii, 96822, USA

³Canada-France-Hawaii Telescope Corporation, Kamuela, Hawaii, 96743, USA

proved to be deep surveys of the same fields at every wavelength possible, so that as complete a SED as possible can be determined for a large number of objects. At radio wavelengths, the VLA at 20cm is the workhorse instrument. The large field-of-view, high sensitivity and good spatial resolution allow images with thousands of sources per pointing and ~ 1.5 arcsecond resolution. New computing algorithms combined with the current generation of fast computers have unlocked this potential of the VLA, which has been there for 25 years.

The μJy radio sky gives unique information about the evolution of faint, distant galaxies from the synchrotron emission observed from both star-forming and AGN-dominated systems. This complements data from other wavelength bands. The ratio of radio to FIR luminosity has the potential to tell us whether star-formation or AGN are dominant (e.g., Yun Reddy & Condon 2001). For star-forming systems the physical size of the emitting regions and their relation to brightness distributions in other bands can tell us about the extent of the star-forming regions independent of dust extinction and perhaps can tell us if a wind is required. Radio AGN are dominantly radio jets and thus tell us about the mechanical energy flowing away from the black hole, instead of the radiation dominated emission seen at other wavelengths. Radiation and mechanical energy dominated AGN may result from different phases of the black hole growth (Churazov et al. 2005; Sijacki et al. 2007) and thus it is important to study both types of AGN. The sensitivity of this survey reaches a surface density of several sources per square arcminute and thus allows us to study a large sample of distant galaxies with only one pointing of the VLA. In this paper we report the results of the radio survey only. Other related papers will discuss the observations at other wavelengths and what we can learn by combining all the data on the objects in this field.

2. Selection of the Field

The field for these observations was selected from the nearly 50 square degrees observed in the SWIRE legacy survey (Lonsdale et al 2003). The goal was to select the best location in this survey for a deep radio field. The Lockman hole area of the survey was chosen due to its uniquely low HI column density and IR cirrus. This makes it ideal for the Spitzer IR observations and followup in many other wavelength bands. The declination of this region is also ideal for a VLA 20cm synthesis since the current VLA 20cm system temperature increases below 50 degrees elevation and long tracks can be observed above this limit in the Lockman hole. The NVSS survey (Condon et al. 1998) was searched for a pointing center with a minimum number of strong sources which would fall within the VLA primary beam and its first sidelobe. The region was also required not to have sources as strong as a Jansky within a few degrees of the field center. The best field was centered at the J2000.0 coordinates

of $10^h46^m00^s$, $59^\circ01'00''$.

3. Observations, Reduction and Cataloging

Observations were made with the VLA in A, B, C and D configurations for a total of almost 140 hours on-source between December 2001 and January 2004. In table 1, we summarize the parameters of the observing runs. Since the total time is dominated by the A configuration, the final image for analysis had a resolution ~ 1.6 arcsecond. The data were all taken in spectra line mode 4, which provides seven 3.125 MHz channels in each of 2 IFs (centered at 1365 and 1435 MHz) and each of two polarizations. Five second integration times were used in the A and B configurations and 10 seconds in the C and D configurations. The integration times and channel bandwidths were chosen to minimize tangential and radial smearing of the images away from the field center. This combination of parameters produces the best compromise for imaging sensitivity and quality possible with the current VLA correlator which dates from the 1970's. This means that there is radial smearing of the image due to the finite bandwidths of the channels which does degrade the images away from the field center and which we will need to take into account in the analysis of the image. Currently the EVLA project is replacing the correlator, receivers and associated electronics on the VLA. By the end of the project now scheduled for 2012, much wider bandwidths and narrower channels will allow more ideal images as well as five to ten times higher sensitivity. Another important consideration for deep VLA work at 20cm with the present system is that the system temperature increases as function of zenith distance due to increased ground pickup due to the undersized VLA L-band feed. For this reason almost all the observations were scheduled within 3.5 hours of source transit to minimize this effect. This problem will also be dramatically improved with the coming of the EVLA.

3.1. Calibration & Editing

All the radio reductions use the AIPS package. Since the total bandwidth is relatively large for a spectral line experiment, for each daily observation we first split a bright point source calibrator from the raw database and applied a phase self-calibration. Then we used this otherwise uncalibrated source to calculate a bandpass correction before we proceeded with the rest of the regular continuum calibration. Regular continuum calibration then continued, using the bandpass calibration to flatten the spectral response, and thus avoid the effects of the raw, sloping spectral response. Calibration was made in the standard way to the Baars flux density scale (Baars et al. 1977) using 3C286 as the flux calibrator.

The weights associated with each integration were also calibrated as a function of observed system temperature as part of the standard AIPS processing. The calibrated dataset was first clipped using the AIPS program CLIP well above the total found flux density found in the field from lower resolution observations in order to remove a few high points before beginning the self-calibration process.

3.2. Imaging & Self-calibration

The D-array data were first imaged to radii 8 degrees outside the field center. The field was chosen to minimize the effect of confusing sources; however, thirty-four confusing sources outside the primary beam were identified which needed to be imaged outside the main mosaic to optimize the final image. The most distant source which was included in the deconvolution is 1.8 degrees from the field center.

For the A-configuration data on the first day, the entire primary beam was then imaged using the AIPS task IMAGR and the 3D, multi-facet options. Besides 37 facets, each with 1000×1000 points, to describe the primary beam, another 34 facets, each with 500×500 points, were centered on all the confusing sources outside of the central region. After initial imaging, each detected source had a tight clean box placed around it to limit cleaning to real features. This procedure allows each image to be cleaned down to the 1σ level and the resulting clean components to be used in the self-calibration process. This process also eliminates almost all of the clean bias and does not artificially reduce the noise on the image as happens when one does not use boxes. The images were self-calibrated, first just in phase, and later in both amplitude and phase using the AIPS task CALIB. These 71 images from the first day were then used as a fiducial image to “self-calibrate” the remaining 16 days of A-array observations. The B, C, and D configuration observations were also bootstrapped to the fiducial images in the same way. Editing was carried out before and during the self-calibration process using both TVFLG and CLIP. Before self-calibration visibility points with amplitudes much larger than the total flux density in the field were removed with CLIP. After each self-calibration step the clean model was subtracted from the calibrated data and high residuals were deleted with TVFLG. Care was taken not to remove moderately high points on the shortest baselines which might represent data not well described by the model.

Since the data-volume from the 140 hours of observations is so large and for the A and B configuration the same hour angles were observed on several days, the next step was to compress the data as much as possible before imaging. This was accomplished using a multi-step process in AIPS which first converted all the times into hour angles using TI2HA. Next the data for each configuration were combined using DBCON and finally UBAVG was used

to average together visibilities with uv coordinates on each baseline close enough together to create negligible effect on the imaging. In practice it is necessary to edit the date in the header for each day’s data and to perform the appropriate sorting to make this process work. However, when the process is finished the full dataset was approximately ten times smaller. This entire process, developed for this survey, has now been combined into the AIPS procedure called STUFFR.

The four configurations were then combined using DBCON in order to make the final images. Of course, since the data were obtained over a period of more than a year, intermediate images were produced when the data for each new configuration was obtained. Many experiments were performed as to the best weighting, the optimum taper and the imaging algorithm to use. In particular, multi-scale clean in IMAGR was found to be most effective until the B configuration was added to the A, C, and D data which were available earlier. However, for the final image, a single resolution clean worked best. The box file for the image was also improved many times during the process of learning about the dataset. It was found that the best images were produced with a set of boxes covering every source that could be recognized in the field.

The images produced in this manor are still affected negatively by the pointing changes on outlying bright sources. This is primarily due to the fact that the two circular polarizations have different pointing centers (*i.e.* beam squint) on the VLA due to the slightly off-axis location of the feeds. This combined with the alt-az geometry of the telescopes causes effective gain on a source far off-axis to vary with hour angle. Also the slightly different frequencies of the two IF’s caused a slightly different primary beam size and thus a source far from the field center has a higher gain at the lower frequency.

As a final step to correct approximately for these two effects, the uv datasets were split into their separate IF’s (2), polarizations (2) and HA ranges (2). Then they were imaged and self-calibrated separately. Finally the eight images of each facet were combined, weighting each by $1/rms^2$ to form an optimum final image. The 37 facets covering the main lobe of the primary beam were then combined into a single image using FLATN. As a final step to produce the most uniform background MWF was used to flatten the image further using the MODE over a 101×101 -pixel support window. This final image has a local *rms* of typically $2.7 \mu\text{Jy}$ over regions 100 pixels in diameter before correction for the primary beam. The pixel size is 0.5 arcsecond and the clean beam is 1.63×1.57 arcsecond at a position angle of 10 degrees.

3.3. Cataloging

The inner 40×40 arcminute region of the final image was chosen for cataloging and further study. This region covers almost the entire useful area of the primary beam. Since the bandwidth of each channel smears the image radially by approximately $0.00223 \times$ (the fractional bandwidth) \times (the distance from the field center), this effect needs to be taken into account in analyzing the images. The smearing becomes comparable to the clean beamsize 12 arcminutes from the field center. Furthermore, as will be seen, the median size of the sources in the field is only a little smaller than the clean beam. Thus for both instrumental and physical reasons, in order to catalog the many sources as possible, it is necessary to analyze the image with more than one resolution. This was accomplished by convolving the full resolution to an effective circular clean beam size of 3.0, 6.0 and 12.0 arcseconds. Each of the four resulting images was then analyzed separately and the results collated and compared. In practice, none of the sources had their best detection in the 12.0 arcsecond image.

The AIPS program SAD was used for forming the initial source lists down to peak flux densities. A catalog for each image was formed down to a peak signal/noise (S/N) of 4.0. The residual images from SAD were then searched to find any remaining sources missed by the program with a S/N greater than 5.0. For sources with a S/N close to 5.0, the fitting process was repeated by hand with JMFIT, using the local *rms* estimate over a region 100 pixels in diameter. In this way a reliable list of sources with S/N of 5.0 or greater at each resolution was compiled. Only sources with peak $S/N \geq 5.0$ in one of the three images (1.6", 3", 6") are included in the final catalog. For both SAD and JMFIT, the smearing due to the finite bandwidth was included in the fitting process.

The catalogs created this way were then collated. The relative noise level varies for each source as a function of distance from the field center, which imposes a selection effect on the final catalog which we discuss later. The results for each resolution image were then compared and the best fit was selected. If the peak S/N was more than 10% higher on the lower resolution image then that result was used. Finally, if the total flux density of the source was significantly larger at lower resolution then that result was adopted. In cases where the results appeared inconsistent, the images were examined to resolve the issue. If a source had a lower limit major axis from the best fit consistent with zero, then the source was assumed to be a point and the peak flux density is used as the estimate of the total flux density. For sources only slightly resolved by this criteria, the total flux density from the fit was cataloged. For unresolved sources, simulations have shown that the fitted peak flux density for the unconstrained, Gaussian functions fitted with JMFIT is the best estimate to the total flux density (Greisen 2002). For sources clearly much larger than the clean

beam, TVSTAT was used to estimate the total flux density and the associated error given the number of beams included in the sum. TVSTAT operates by the user drawing a region around the emission region then summing the total signal in the region. Errors in the flux density and position were calculated using the formalism of Condon et al. (1998). A noise term proportional to the total flux density of 3% is included for each source to account for any calibration errors and the uncertainty is in the primary beam correction. This percentage error is consistent with the ratios of our flux densities to the NVSS flux densities of sources > 5 mJy which are in the field.

4. Results

4.1. Radio Catalog

In table 2, we give the first ten lines of the radio catalog, while the rest is provided electronically. Column (1) contains the source number. If the source has a number less than 2000, then it was found in the original list found with a $S/N \geq 5.0$ from running SAD on the full resolution image. Sources with numbers ≥ 10000 were found in lower resolution images or in checks of the residual images. Columns (2) and (3) contain the radio RA and Dec along with the estimated error. Column (4) contains the observed (uncorrected) peak flux density from the map in μJy per beam. In column (5) we list the corrected total flux density and estimated error. Column (6) contains the peak S/N . The error for column (4) can be recovered by dividing column (4) by column (6). We give the S/N as opposed to the error since the S/N was used to define the catalog cutoff and later is used in the calculation of $\log N - \log S$. In column (7), we give the best fit deconvolved size in arcseconds. If a resolved two dimensional Gaussian was the best fit, we give the major and minor axis size (FWHM) and the position angle. Upper limits are given for sources which were unresolved based on the results of JMFIT or SAD. For sources with very large sizes, as shown in figure 1 and 2, sizes and total flux densities were estimated directly from the images using the AIPS tasks, IMVAL and TVSTAT.

4.2. Angular size distribution

This deep survey contains information about the angular size distribution as a function of flux density. However, our limited survey brightness sensitivity means that we will miss larger sources near the survey limit. We also have limited ability to determine source sizes for sources much less than one arcsecond in size. However, our Gaussian fits show that

we resolve about half the sources we detect. This allows us to give a good estimate of the median source size. In a later paper we will discuss the linear size distribution. However, just from the radio image the angular size distribution gives us a hint about the nature of the faint source population. Also as we survey to deeper limits we can learn more about the interesting angular sizes for future radio instruments as well as whether we may reach a natural confusion limit where the sources themselves may overlap and thus limit our ability to study fainter sources.

For the purposes of this investigation we will limit ourselves to the inner part of the image where the image is most sensitive. For the fainter sources, we stay close to the field center and for the relatively rarer, brighter objects we will use a larger area. Sources within five arcminutes of the field center have very small smearing due to the bandwidth effects discussed earlier and the sensitivity over this region is almost unaffected by the primary beam. Of course, there is still a bias against detecting larger sources close to the S/N limit. For brighter sources, the higher S/N makes up for the somewhat larger smearing, so we can measure their sizes more accurately. However, their number density decreases, so we need a larger area for adequate statistics. Table 3 gives statistical properties of each sample subset we analyzed. In column 1 we give the radius from the pointing center in arcmin; columns 2 and 3 contain the minimum and maximum flux densities for the subsample; in column 4 we list the number of sources; columns 5 and 6 contain the mean size and its error from the Kaplan-Meier analysis and column 7 contains the observed median size (uncorrected for incompleteness); in column 8 we list the percentage of resolved sources which went into the Kaplan-Meier analysis.

In figure 3 we show histograms of the Kaplan-Meier estimate of the distribution of fitted Gaussian major axis size versus flux density, using the IRAF task KMESTIMATE for this purpose. The IRAF task allowed us to include the upper limits in the calculation, although most of the sources that we used for this purpose have non-zero detections for the major axis. The primary purpose of this analysis is to determine how the median source size evolves with flux density. Except for the lowest flux density bin for which we quote an upper limit, significantly more than half the sources in each bin are resolved, but in general there are some sources with upper size limits which exceed the median. The Kaplan-Meier formalism provides a way to do a small extrapolation to the median taking into account the upper limits in a consistent way. We then can compare this result with source size distributions found from higher resolution observations. We show the full results of the Kaplan-Meier estimates which are consistent with the data trends but may underestimate the number of very small sources. The histograms show that the maximum source size we detect increases with flux density. Below $100 \mu\text{Jy}$ the cutoff is roughly the largest size we might expect to be able to detect based on surface brightness, although this result depends in detail on the source shape.

Thus below $100 \mu\text{Jy}$ we suspect that we are incomplete for the larger sources, especially below $30 \mu\text{Jy}$. Even if we ignore this effect, the median size for the sources we detect remains above one arcsecond and is larger if we try to correct for the missing population of larger sources. In the $20\text{-}30 \mu\text{Jy}$ bin the median size even appears to increase to 1.5 arcsecond without any corrections. These results are consistent with Muxlow et al (2005) and suggest that the size distribution of the radio population may not continue to decrease below $100 \mu\text{Jy}$ but may level out at a median size > 1 arcsec.

4.3. Log N - Log S

It might seem easy to calculate the density of sources as a function of flux density from a catalog such has been compiled in this paper. However, several effects contribute to make the source list incomplete even at fairly large S/N. The detection rate is obviously directly affected by the primary beam attenuation. However, both the finite bandwidth of each channel (3.125 MHz) and to a lesser extent, the finite time averaging smear the sources as a function of radius from the field center and thus reduce the peak amplitude (see figure 2 of Fomalont et al. (2006)). Furthermore, the fact that the sources have a median source size on the order of the clean beam size, also reduces the completeness of the survey. Thus besides counting the sources as a function of flux density, an incompleteness correction needs to be included in the calculation. Since we do not know the actual distribution in angular sizes as a function of flux density, this correction can only be approximate and based on the properties of sources at higher flux densities. However since we find evidence in the previous section that the median sizes are consistent with being approximately constant as a function of flux density, we will make the simple assumption that the distribution of angular sizes remains constant at flux densities below 1 mJy.

One problem is that most very deep surveys have been carried out using only the VLA's highest resolution at 20cm to avoid confusion and obtain the best possible positions. However, such surveys select against finding large sources and thus our view of the radio sky is biased against large sources. Our survey, while still having some such bias, used all four VLA configurations and thus has the necessary spatial frequencies to detect quite large sources. As outlined earlier we did search for large sources using restoring beams as large as twelve arcseconds. We also are more sensitive than any previous survey, so we are more sensitive to large sources than other VLA deep surveys. However, due to confusion and our overall weighting toward longer baselines, we are not as sensitive to large sources of a given flux density as we are to small sources.

Fomalont et al. (2006) finds that $8 \pm 4\%$ of μJy sources are larger than 4 arcsec. In our

300 – 1000 μJy sample we find that 5/30 or about 17% of our sources are bigger than 4 arcsec. Even in our 30 – 100 μJy sample, we find 4/50 sources are bigger than 4 arcseconds and none are detected which are bigger than 6 arcsec. Assuming that the size distributions are the same as a function of flux density, we should have missed some larger sources in this bin. Thus it seems likely that at least 15% of the sources in our field are bigger than 4 arcseconds. Overall, we find slightly larger sources than Fomalont et al. (2006) and we suspect we might be still underestimating the source size distribution.

4.3.1. Sensitivity vs Distance from the Field Center

In their figure 2 Fomalont et al. (2006) show the sensitivity decreases as a function of distance from the field center of a point source at our full resolution due to the VLA primary beam, the bandwidth smearing due to our 3.125 MHz channels and the time smearing. The latter two effects are due to the smearing of the synthesized beam by our finite time and frequency resolution. These effects can be mitigated by using a bigger synthesized beam. This mitigation is achieved in practice by convolving the cleaned image by the appropriate two dimensional Gaussian to produce the desired new beam size. However, this process increases the noise on the image, so picking the best beam size is a trade-off which changes with distance from the field center. In figure 4, we show the relative point-source sensitivity for the three different resolutions we analyzed. Note that the three arcsecond (red) curve crosses the full resolution (blue) curve about nine arcminutes from the field center and thus beyond this radius the three arcsecond image is actually more sensitive than the full resolution image for point sources.

A further complication is that the sensitivity for resolved sources of different sizes is also a function of beamsize and distance from the field center. In figure 5 we show examples for three different Gaussian source sizes as an example (one, three and seven arcsecond FWHM, thin solid lines, dashed lines and thick solid lines respectively). The one arcsecond sources, the full resolution and three arcsecond resolution curves now cross about 6.5 arcminutes from the field center. For three arcsecond sources, the red (three arcsecond resolution) curve is always above the blue curve. For as large as seven arcsecond, the green six arcsecond curve is always best.

Since most of the sources are large enough to have images significantly bigger than a point source at our highest resolution even in the field center, the clean beam which is most sensitive varies with both distance from the field center and source size. Furthermore depending on the source size we are incomplete at each flux density and peak S/N due to the source size distribution. Since we do not know this distribution in great detail we can

only correct for this affect approximately. In practice, there seem not to be many sources larger than, say, five arcseconds, thus above some flux density we don't miss enough sources to affect the source counts significantly for most purposes. However, at the bottom of the catalog, where the information is most interesting, we must be somewhat uncertain due to not knowing the source size distribution in detail.

4.3.2. *Calculating and Correcting Log N - Log S*

We first calculate the number counts ignoring the source size distribution. For each detected source we calculate the area on the sky over which it can be detected, taking into account the three different resolutions we have used for our cataloging process. In figure 6 we show the log N - Log S results for our survey (blue points) and the results of the shallower SA13 survey (Fomalont et al. 2006) using yellow squares. One can see that both curves turn down at low flux densities but not at the same flux density. This certainly suggests some sort of incompleteness. In order to explore this result, we calculated our log N - Log S for different S/N cutoffs ranging from 5 to 10. These results are shown in figure 7. One can see that the higher the S/N the earlier the higher the flux density at which the curves turn down. The SA13 curve is in good agreement with our S/N cutoffs which approximately match the Fomalont et al. (2006) flux density cutoff. This seems to suggest that the incompleteness in the full catalog comes from some other source than S/N.

At least part of this effect is due to the fact that we are resolving the sources, as discussed in the last section. In order to correct for this effect we need to know the source size distribution in some detail. Clearly we have only a rough idea of the size distribution as a function of flux density. In order to correct for source resolution, we have assumed a size distribution based on the higher resolution results of Muxlow et al (2005) at small source sizes and a large source-size tail based on our results (figure 8), which should be more complete because of our better *uv* coverage on short baselines. We assume this distribution is the same for all flux densities we observe.

Using this assumed size distribution, we can then correct for our incompleteness as a function position and resolution of our images. In figure 9 we show the effect of this correction. The impact is to flatten the counts. The scatter in the estimated source densities is primarily due to the interaction of the size correction and the inverse areas with the S/N cutoffs. If a few sources lie close to the S/N cutoff then they can dominate the estimate and the associated error. In order to minimize this effect in the estimate of log N - log S, we have calculated the corrected log N - log S with cutoffs from S/N=5 to S/N=10 in steps of 0.2 in S/N. Then we have performed a weighted sum of the estimates in each flux density

bin. The results are summarized in table 4 and shown in fig 10. In this plot we can see a flat distribution with flux density for normalization coefficients of the differential $\log N - \log S$. In order to estimate the errors in the new process described above we constructed 100 Monte-Carlo simulations with similar $\log N - \log S$ and the parent angular size distribution we assumed for the analysis. Using our algorithm described above we then used the simulations to estimate the one sigma error bars shown in figure 10. Our result is still subject to errors in our assumed parent size distribution and any cosmic variance; we have not attempted to include these potential sources of error in our error estimate.

The resulting distribution, although dependent on the assumed angular size distribution, is consistent with a flat shape for the normalizing coefficient of the differential $\log N - \log S$ distribution. Thus we find no evidence that the counts are turning down when one takes into account the size distribution and other effects affecting the observations. Since our observed size distribution down to the faintest levels in the survey is consistent with our assumed global size distribution, the results in figure 10 and table 4 are our best estimate of $\log N - \log S$. We have searched our images for sources both with an automatic program and then verified the results by searching the residual images by eye and refitting each source down to a peak S/N of sigma with JMFIT. Thus we do not think we have missed many, if any, five sigma sources. If we have missed sources then our results are underestimates of the counts at the faint end. We see no evidence for a turn-down in the counts or a decrease in source size.

4.3.3. *Comparison with previous $\log N - \log S$ determinations*

In figure 11 we show our new values compared with other recent determinations of $\log N - \log S$ for $S_{20cm} < 1$ mJy. Our approach to cataloging and estimating $\log N - \log S$ is different in detail compared to previous studies. We believe it takes into account the best estimate of the size distribution in a better way than has been used for the other data shown in figure 11. Furthermore, our result is for a single direction in the sky and is, of course, subject to cosmic variance. Nonetheless, while our points are a little higher than the other results, the function is generally flat from 1 mJy down to our lowest point at $17\mu\text{Jy}$. At our survey limit, counting the inferred resolved population, there are ~ 6 sources per square arcminute.

Since there is no trend toward smaller sources at lower flux density, this raises the issue of whether we are approaching the natural confusion limit. If the counts remain flat and the size distribution remains the same, we are less than an order of magnitude from this limit. With the EVLA it should be possible to improve the limit by this factor and test

whether we are approaching this ultimate limit and whether even deeper surveys with a hypothetical SKA will suffer for this fundamental problem. However, the details of the radio source structure remain interesting even if the natural sources confusion is approached. Since the typical source is ~ 1 arcsecond in size, this argues for any next generation continuum survey array to be designed for high spatial resolution, perhaps $\sim 0.1 - 0.01$ arcsecond and to concentrate on source structure and its spatial relation to high resolution results at other wavelengths, not deep detection surveys.

5. Conclusion

We have presented the deepest image so far of the radio sky in terms of source density and provided an electronic catalog for sources with peak signal-to-noise ratios > 5 . The median size distribution for these sources continues to be ~ 1.2 arcseconds or a bit larger down to the bottom of the catalog. After a correction for incompleteness due to source size, we find that the $\log N - \log S$ normalization factor remains approximately flat down to $15\mu\text{Jy}$, corresponding to about six sources per square arcminute. If this trend continues the 20cm natural confusion limit may be reached near one μJy .

REFERENCES

- Baars, J. W. M., Genzel, R., Pauliny-Toth, I. I. K., & Witzel, A. 1977, *A&A*, 61, 99.
- Biggs, A. D. & Ivison, R. J. 2006, *MNRAS*, 371, 963.
- Churazov, E., Sazonov, S., Sunyaev, R., Forman, W., Jones, C. & Bohringer, H. 2005, *MNRAS* 363, 91.
- Condon, J. J., Cotton, W. D., Greisen, E. W., Yin, Q. F., Perley, R. A., Taylor, G. B., & Broderick, J. J., 1998, *ApJ*, 115, 1693.
- Fomalont, E. B., Kellermann, K. I., Cowie, L. L., Capak, P., Barger, A. J., Partridge, R. B., Windhorst, R. A. & Richards, E. A. 2006, *ApJS*, 167, 103.
- Greisen, E. C. 2002, private communication.
- Huynh, M. T., Jackson, C. A., Norris, R. P., & Prandoni, I. 2005, *AJ*, 130, 1373.
- Lonsdale, C. J. and 36 coauthors 2003, *PASP*, 115, 897.
- Muxlow, T. W. B., Richards, A. M. S., Garrington, S. T., Wilkinson, P. N., Anderson, B., Richards, E. A., Axon, D. J., Fomalont, E. B., Kellermann, K. I., Partridge, R. B., & Windhorst, R. A, 2005, *MNRAS*, 358, 1159.
- Sijacki, D., Springel, V., di Matteo, T., & Hernquist, L. 2007, *MNRAS*, 380, 877.
- Yun, M. S., Reddy, N. A. & Condon, J.J. 2001, *ApJ*, 554, 803.

Table 1. Observing Runs Summary

Configuration	Startdate	Enddate	Hours
A	02Jan27	02Mar11	104.0
B	03Dec15	04Jan14	27.5
C	03Jan06	03Jan06	6.5
D	01Dec15	01Dec15	1.6

Table 2. Radio Source Catalog

Name	RA(2000.0)	Dec(2000.0)	Peak $\mu\text{Jy}/\text{b}$	Total μJy	S/N	Size arcsec
00004	10 43 19.29(0.04)	59 08 42.6(0.3)	35.7	394.4(43.1)	13.7	2.1x0.4p=109.
00005	10 43 20.06(0.07)	58 51 42.3(0.6)	14.1	141.9(27.0)	5.4	<3.5
00006	10 43 20.63(0.57)	58 56 20.8(4.4)	227.3	42293.0(4343.5)	71.0	146.
00007	10 43 20.84(0.05)	58 53 50.4(0.4)	27.3	167.7(21.5)	21.5	<3.3
10007	10 43 21.84(0.03)	59 12 54.4(0.2)	24.4	213.7(30.1)	7.6	<3.1
00010	10 43 23.44(0.02)	59 17 50.8(0.2)	29.9	482.7(58.0)	9.2	<2.7
00012	10 43 25.05(0.02)	59 06 16.1(0.2)	108.4	653.5(43.6)	33.8	1.7x1.3p=45.
00013	10 43 26.79(0.06)	59 01 47.7(0.5)	32.0	330.2(37.4)	12.4	2.6x1.4p=81.
20013	10 43 26.81(0.02)	58 55 43.0(0.2)	25.1	123.0(16.9)	7.8	<3.4
00015	10 43 28.02(0.02)	59 13 05.8(0.2)	27.2	211.4(27.4)	8.4	<2.4

Table 3. Source Size Summary

Radius arcmin	Minimum μJy	Maximum μJy	Sources	Mean arcsec	Error arcsec	Median arcsec	Resolved %
5	13	20	21	0.9	0.2	<1.5	19
5	20	30	36	1.6	0.1	1.5	58
5	30	100	51	1.6	0.2	1.1	75
10	100	300	29	2.3	0.6	1.0	72
20	300	1000	30	2.6	0.7	1.1	83

Table 4. Differential normalized source counts for 1046+59. The table contains 1) S_l (the lower flux density limit of the bin), 2) S_h (the upper flux density limit of the bin), 3) the normalization factor and its error.

S_l	S_h	$S^{2.5}dN/DS$
μJy	μJy	$\text{Jy}^{1.5}\text{sr}^{-1}$
15	19	6.48 ± 1.51
19	24	6.50 ± 0.89
24	36	6.11 ± 0.58
36	54	5.75 ± 0.69
54	100	7.01 ± 0.74
100	150	6.24 ± 1.11
150	300	4.46 ± 0.94
300	1500	4.23 ± 1.26

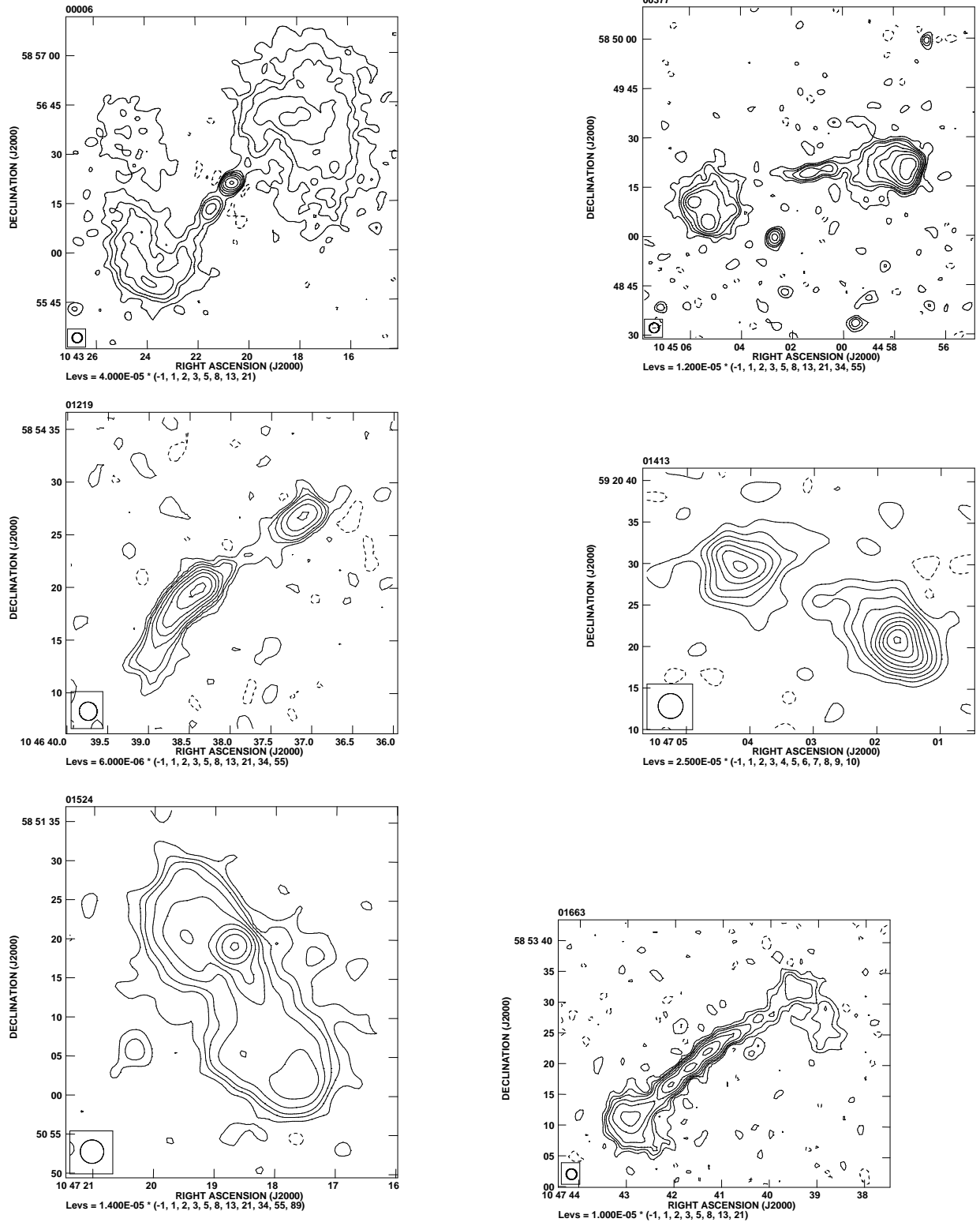


Fig. 1.— Extended Sources—Contour Levels in Jy

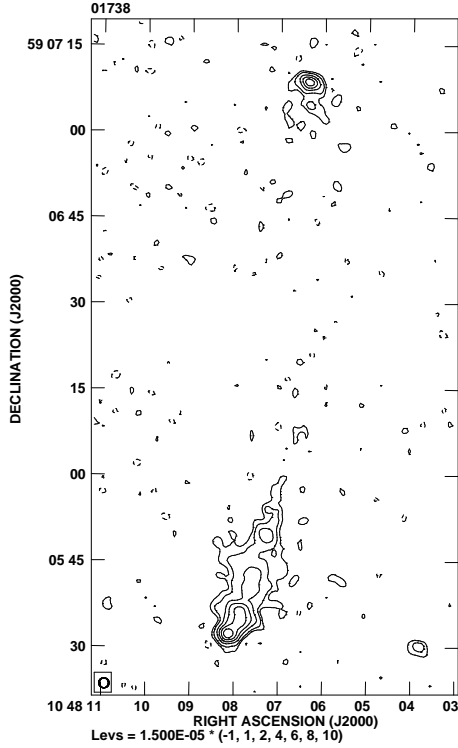
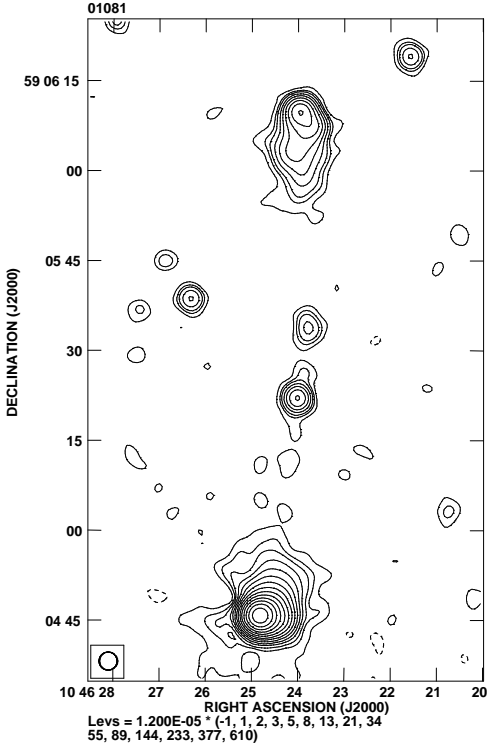
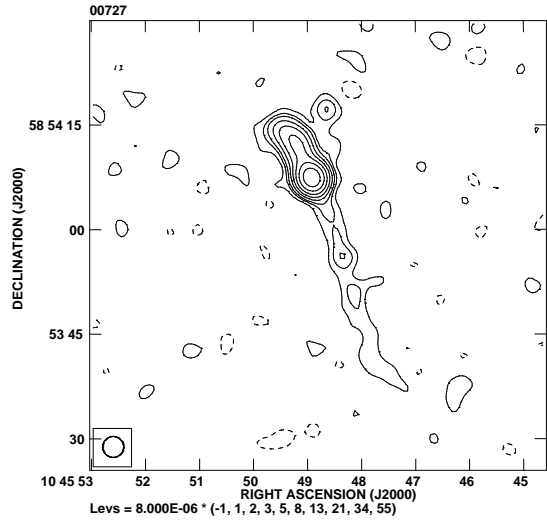
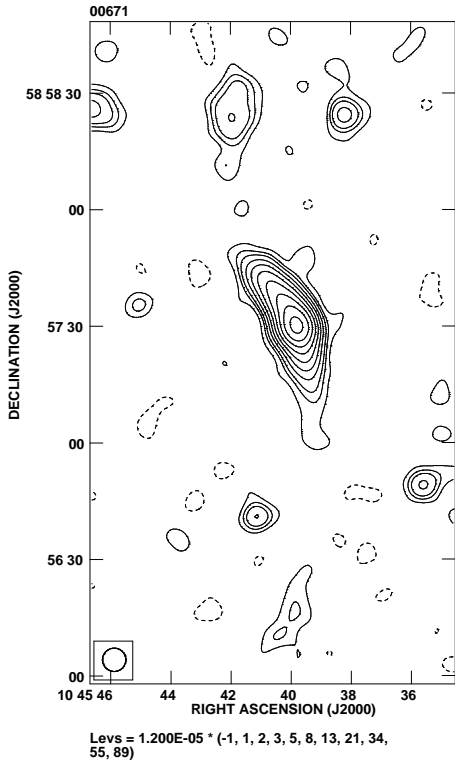


Fig. 2.— Extended Sources—Contour Levs in Jy

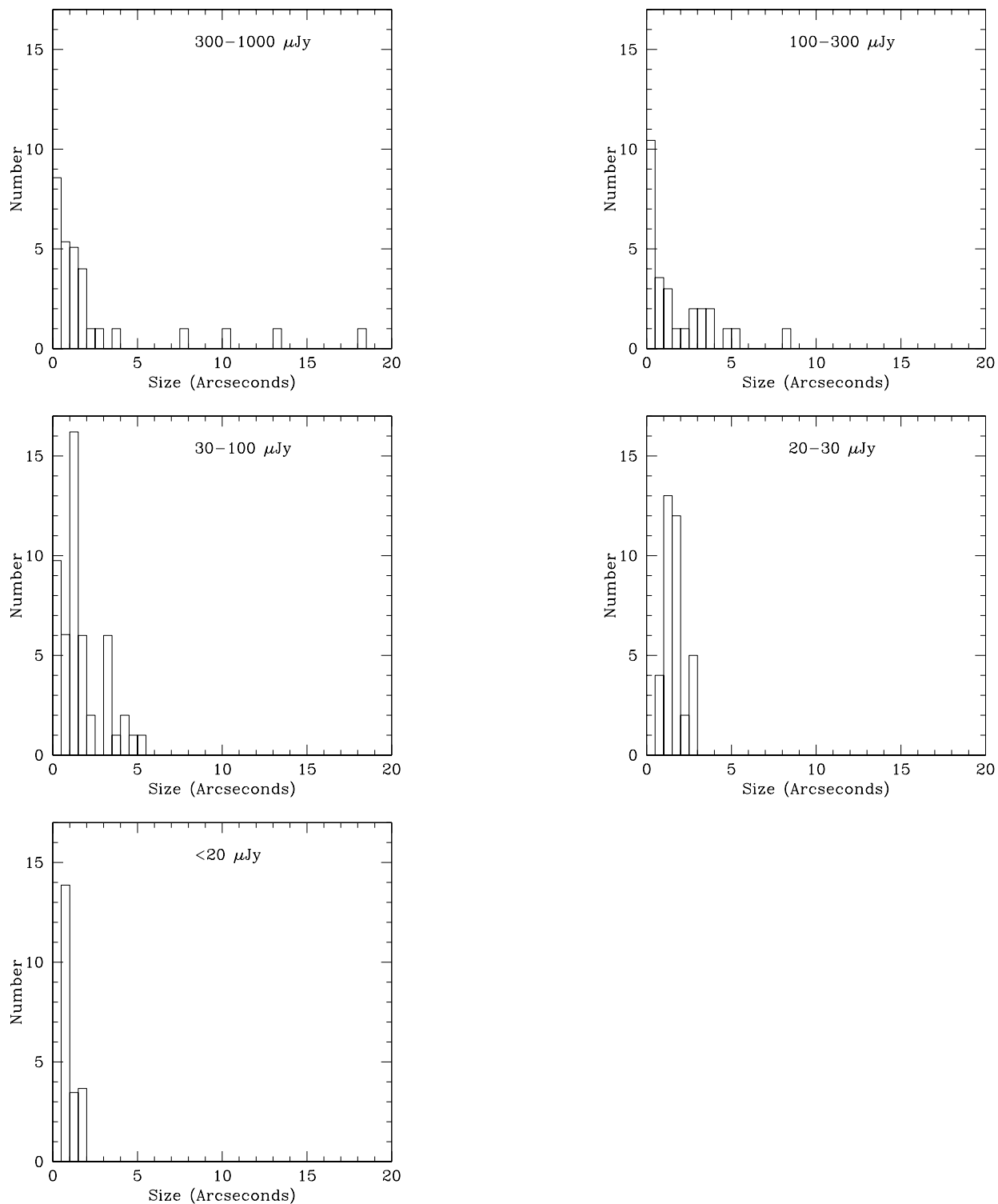


Fig. 3.— Histograms of the Kaplan-Meier estimates of the deconvolved angular-size vs flux density for various ranges in flux density. Note that the Kaplan-Meier formalism may have underestimated the number of very small sources where it is poorly constrained but likely gives a good estimate of the median size.

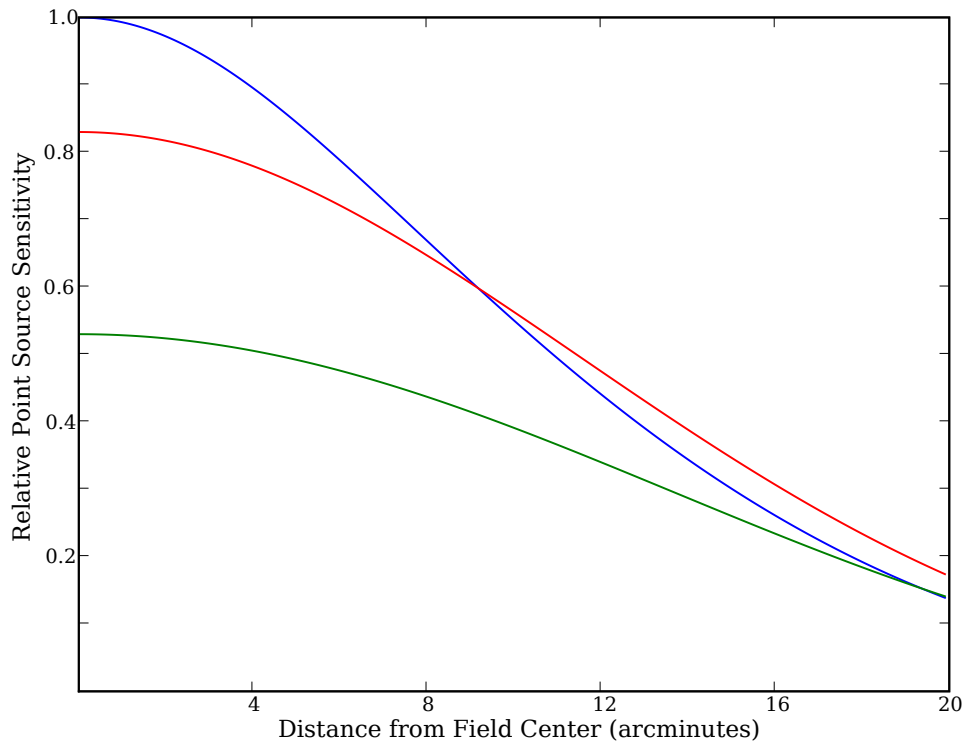


Fig. 4.— Relative point-source sensitivity as a function of distance from the field center for the three image resolutions used for cataloging: blue: full resolution ($\sim 1.6''$), red ($3.0''$), green ($6.0''$).

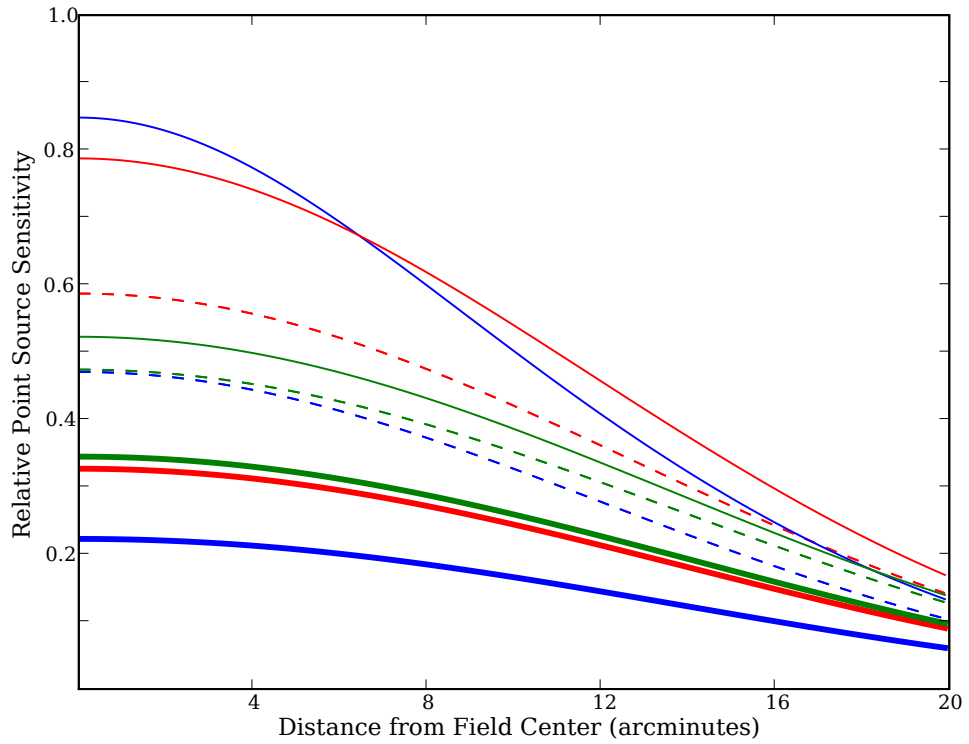


Fig. 5.— Relative sensitivity for the three different image resolutions and three different source sizes: As in fig 4 blue: full resolution ($\sim 1.6''$), red: ($3.0''$), green ($6.0''$). The line solid lines are for a source of $1''$ Gaussian FWHM; dash lines, a $3''$ FWHM and thick solid lines, $7''$ FWHM.

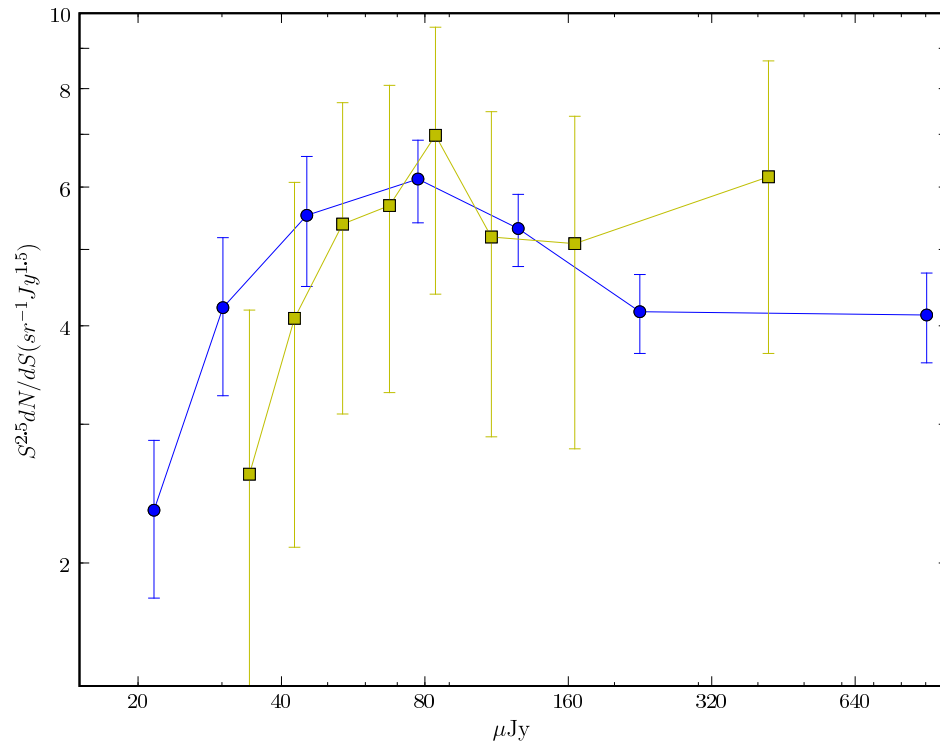


Fig. 6.— The log N - Log S differential distribution uncorrected for source resolution for our survey (blue dots) and the SA13 field (yellow squares).

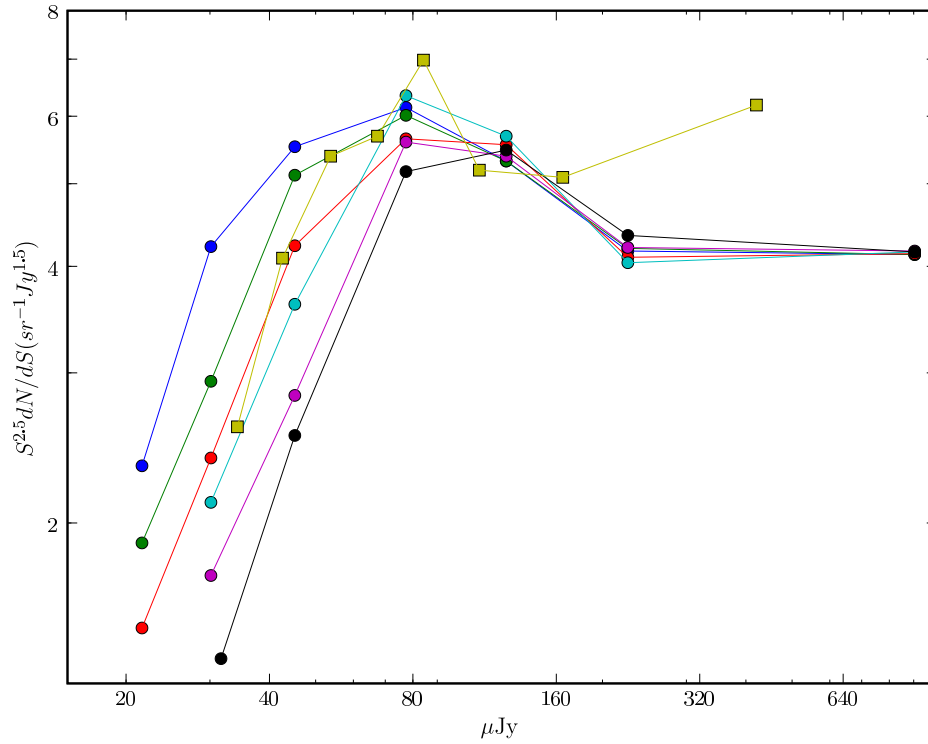


Fig. 7.— The uncorrected log N - log S for our survey with various S/N cutoffs (dots) and the SA13 results (yellow squares). For our survey the curves are S/N= 5(blue), 6(green), 7(red), 8(cyan), 9(magenta) and 10(black). Note that all the curves turn over at low flux densities but that the turnover shifts to higher flux densities with higher S/N.

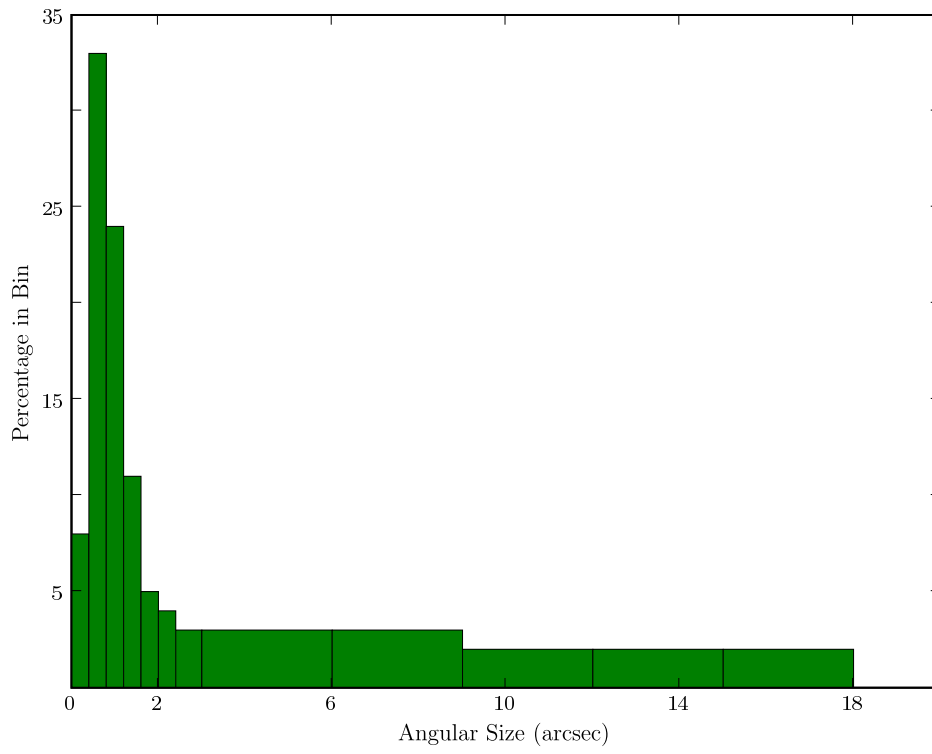


Fig. 8.— The adopted angular size distribution used to correct the log N - log S counts. Note that the percentages shown are for the bin shown and are not normalized to a uniform bin size in arcseconds.

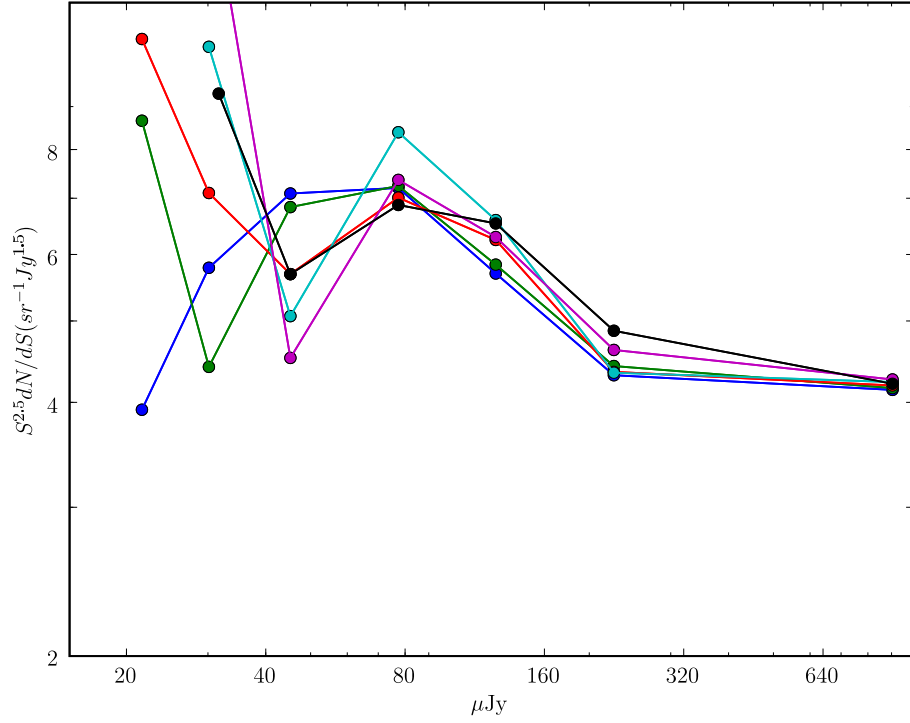


Fig. 9.— The corrected log N - log S for our survey with various S/N cutoffs (dots). The respective curves are S/N= 5(blue), 6(green), 7(red), 8(cyan), 9(magenta) and 10(black).

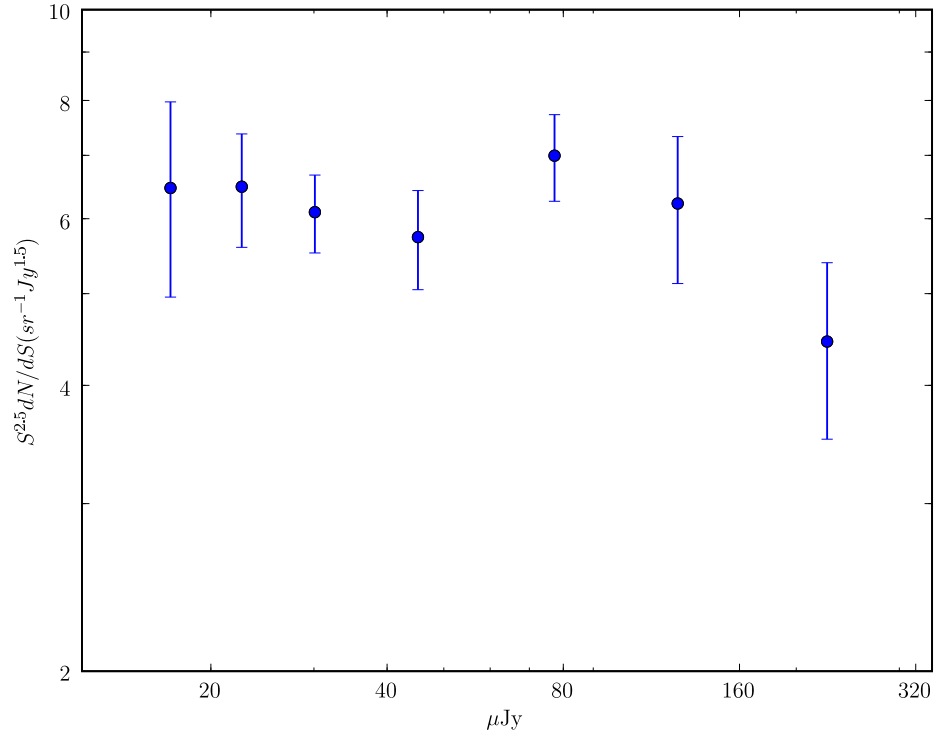


Fig. 10.— Our final, corrected log N - log S using the weighted sum of the estimates from our sliding cutoff window as described in the text. The error bars were determined from Monte Carlo simulations.

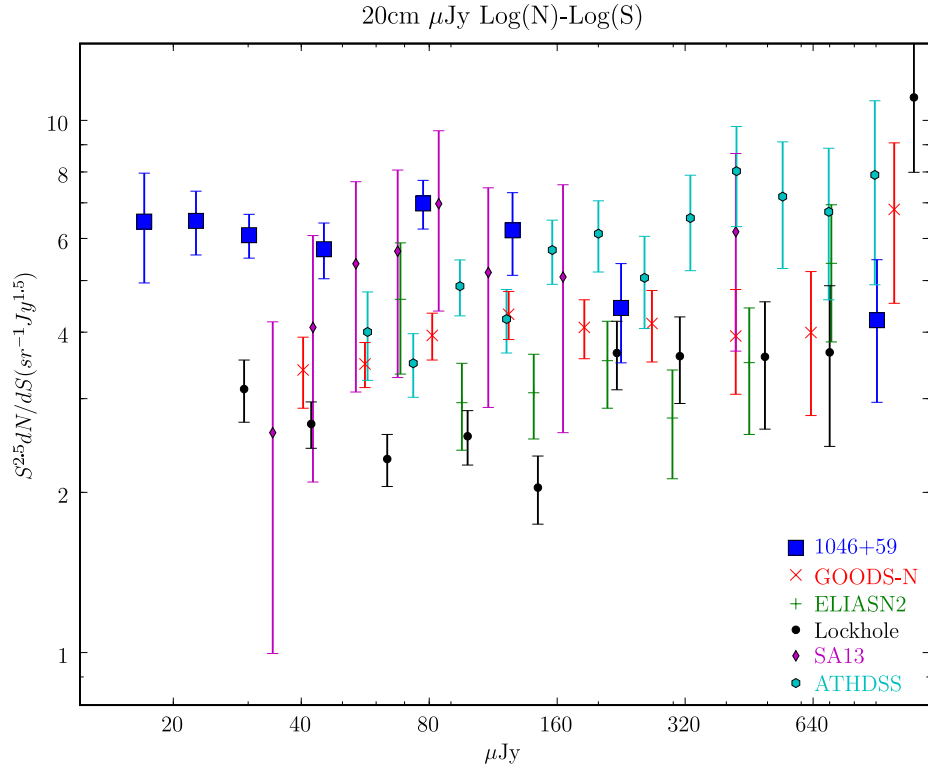


Fig. 11.— Recent log N - log S estimates for $S_{20\text{cm}} < 1$ mJy. The 1046+59 points are from this paper; the GOODS-N, ELIASN2, and Lockhole points are from Biggs & Ivison (2006); SA13 data are from Fomalont et al. (2006); and ATHDSS data are from Huynh et al. (2005).